PCCP
Physical Chemistry Chemical Physics

Accepted Manuscript

This article can be cited before page numbers have been issued, to do this please use: T. Sasaki, M. Nakamura and Y. Ohshima, *Phys. Chem. Chem. Phys.*, 2026, DOI: 10.1039/D5CP04295J.

ROYAL SOCIETY OF CHEMISTRY

rsc.li/pccp

View Article Online
DOI: 10.1039/D5CP04295J

PCCP

ARTICLE TYPE

Cite this: DOI: 00.0000/xxxxxxxxxx

Six-dimensional intermolecular potential energy surface and vibrational states of the benzene–methane vdW complex

Toru Sasaki,[a] Masaaki Nakamura,[a] and Yasuhiro Ohshima*[a]

Received Date
Accepted Date

DOI: 00.0000/xxxxxxxxxx

We have developed a six-dimensional (6D) model to describe the intermolecular potential energy surface (IPS) pertinent to binary van der Waals (vdW) complexes composed of a benzene (Bz) and a small molecule X. In the present formalization, termed Coupled-Stretch-Bend-Internal-rotation (CSBI) model, the longitudinal displacement of X from the Bz plane (as vdW stretch), the 2D displacements of X parallel to the Bz ring (vdW bend), and the 3D internal rotation of X inside the complex are taken as internal coordinates, and the IPS is composed of symmetry-adapted terms, which are expanded as explicit functions of the coordinates. Here Bz–methane has been chosen to apply the model because of its importance to gain detailed understanding on the C–H/π interaction. Quantum chemical calculation at the CCSD(T)/aug-cc-pVTZ level of theory has been conducted to obtain single-point energies of 525 grids for various complex conformation, and the calculated results have been processed with the least-squares regression to determine potential parameters in the CSBI model. The IPS thus constructed has shown that in the most stable conformation the methane resides on the aromatic ring (with the intermolecular distance of 3.712 Å), pointing one of its C–H bond to the center of the Bz ring. The barrier for the internal rotation along the minimum energy path is moderately low (of 57 cm^{-1}). The IPS exhibits substantial coupling between the three coordinate spaces, and effects of such mode coupling can be visualized as the difference in the potential profiles with and without the coupling terms. Eigenstates for the intermolecular motion have been determined by diagonalizing the full Hamiltonian matrices with the CSBI potential. Character of each eigenstate is assessed by examining its composition projected onto the basis functions as well as vibrationally averaged geometrical parameters.

1 Introduction

Noncovalent forces pertinent to an aromatic ring are pivotal to the properties of solids, solutions, and interfaces involving aromatic molecules as well as conformation and functionality of bio- and artificial supramolecules.[1–3] Binary van der Waals (vdW) complexes, Bz–X, composed of benzene (Bz) with a small molecule X, are ideal models for the noncovalent interaction.[4–8] In particular, Bz–X with X = methane has been extensively studied with the aim of achieving truly microscopic description of the C–H/π interaction by experiments[9–13] and theory.[14–19] Forces between the two constituents of binary molecular systems can be fully characterized once the intermolecular potential energy surfaces (IPSs) of the systems are determined.[20] Hence constructing *chemically* accurate IPSs and gaining detailed insight into the intermolecular vibrational dynamics on them is the central subject in the studies of vdW complexes.[4,8,20]

IPSs pertinent to most vdW complexes (including Bz–Xs) are so anharmonic that normal mode description is totally inadequate.[5] All the intermolecular degrees of freedom have to be considered simultaneously due to substantial coupling among them and a wide range over the full coordinate space (with dimension of up to 6) has to be explored to cover feasible geometrical configurations. For binary vdW complexes exclusively containing small molecules, highly reliable IPSs have already been reported in recent studies, where intramolecular vibrational degrees of freedom have also been taken into consideration in some cases.[21–27] The protocol adopted herein can be summarized as follows. First, high-level quantum chemical calculation is conducted to evaluate the energies for various relative geometries of the two constituents. Next, the results from the single-point energy calculations are fit to an appropriate model function to give an analytical representation of the IPS. Then, the constructed IPS is assessed by the comparison with spectroscopic constants calculated on the basis of the IPS with the results from experimental observation. If needed, the IPS is refined to provide better agreements with the experiments. Many studies have also been devoted to the con-

[a] *The Department of Chemistry, School of Science, Institute of Science Tokyo, 2-12-1-W4-9 Ookayama, Meguro-ku, Tokyo, 152-8550 JAPAN; E-mail: ohshima@chem.sci.isct.ac.jp*

View Article Online
DOI: 10.1039/D5CP04295J

struction of IPSs for Bz complexes with a rare-gas atom.[28–35] Application to Bz–X with X = molecules, however, has been sparse, probably due to higher demands for calculation caused by the increase of dimensionality for the intermolecular motion. To date, two complexes with X = N_2 and water have been studied.[36–39]

For accurate construction of IPSs and efficient computation of intermolecular dynamics, it is essential to use a suitable coordinate system and an appropriate functional form for the IPS. In general, relative motion of two rigid bodies is defined with distance between the centers of mass of the bodies and two sets of Euler (or polar) angles to represent the orientation of each body.[20,40] In the spherical expansion,[40] an IPS is expanded with a series of the spherical harmonics or rotational matrices with the angles as variables. When anisotropy, i.e., angular dependence of the IPS, is not substantial as in most binary systems composed of small molecules, the spherical expansion is quickly converged and internal-rotation wave functions can be used as suitable basis sets to represent the angular motion of both the molecules inside the complex.[40,41] However, in Bz–X systems, the radial-angular coupling is so extensive because of the bulky flat shape of Bz that the Euler angles for Bz are inadequate as coordinates to represent the intermolecular motion. Since X is located on top of the Bz ring in most low-energy parts of the IPS in Bz–X, three dimensional (3D) displacements of X relative to the Bz plane (plus the Euler angles for X if X = molecule) have been commonly used as internal coordinates in Bz–X.[28–39] In early studies on Bz–Ar, the IPS has been expanded in the polynomials of the coordinates (called Morse-type potential).[28,29] Other recent studies have adopted more sophisticated functional forms based on the site–site model, where the total potential energy of the system is represented as a sum of pair potentials between atoms out of each molecule (with higher-order corrections for many-body interaction).[30–39] With the site–site model, the dynamical calculation becomes much more tedious since matrix elements for the IPS should be numerically computed with the basis functions represented with the internal coordinates.

We have recently been working on the construction of an accurate IPS and the attainment of detailed insight into the intermolecular vibrational dynamics in the Bz–methane complex. We have chosen the system as most suitable to be explored with the following multiple reasons. First, the complex deserves the significance as a prototypical model for the C–H/π interaction as mentioned before. Second, while the previous theoretical studies have explored its IPS in limited dimensionality,[14–19] construction of a 6D IPS will be highly valuable. Third, since it possesses maximum intermolecular degrees of freedom as binary systems, a model extendable to various other Bz–X systems can be developed through consideration of Bz–methane. Fourth, the computational cost can be kept reduced owing to high geometrical symmetry in the IPS of the system. In the present report, we present a theoretical part of our study. Here we have developed a new functional form, called Coupled-Stretch-Bend-Internal-rotation (CSBI) model, to describe the IPS of Bz–X. In the present model, the longitudinal displacement of X from the Bz plane (usually referred to as vdW stretch), 2D displacements of X parallel to the Bz ring (vdW bend), and 3D internal rotation of X inside the complex are utilized as the internal coordinates, as in the previous studies.[36–39] Then, the IPS is composed of symmetry-adapted terms, which are expressed as explicit functions of the coordinates. It has to be noted that this model potential is not suitable to describe the global IPS covering whole coordinate space. For instance, conformation with X far away from the figure axis of Bz cannot be represented adequately with the model. Still, it affords us accurate description on most low-energy parts of the IPS accessible via spectroscopic investigation. More importantly, this model provides a direct correlation of the coupling among motion along different coordinates with the potential parameters for the terms in the expanded series, and we can gain an intuitive picture on the highly coupled intermolecular motion of the system.

This paper is organized as follows. Succeeding the Introduction, the second section describes the theoretical framework of the CSBI model. The beginning part introduces concisely the coordinate system adopted herein and rest of the section is devoted to formal derivation of the CSBI potential and detailed description of the potential for Bz–methane. The third section explains computational details to construct a CSBI potential via high-level quantum chemical calculation. Intermolecular vibrational energy levels are also computed with the determined CSBI potential. The fourth section represents results and discussion. The determined potential parameters are listed and various 2D cross sections of the potential are visualized to represent mode coupling between the stretch, bend, and internal rotation. Energy-level structure of the fully coupled 6D motion is also illustrated, and characterization of each energy level is conducted by examining basis-function composition and root-mean-square amplitudes of the vibrational coordinates. The fifth section concludes the theoretical part of our study. The forthcoming paper will report the experimental part of the study on intermolecular vibrational energy levels via frequency- and time-domain spectroscopy. The experimental results will be compared with those calculated in the present paper.

2 Construction of the CSBI model

2.1 Coordinate system

Before discussing the IPS in Bz–X, We first define the internal coordinate system that describes the intermolecular motion. Here we assume both the Bz and X molecules as rigid bodies and do not consider intramolecular vibration. Then, we employed the cylindrical + Euler angle coordinates, a system previously utilized in other Bz–X researches.[36,38,42] As shown in Fig. 1, we first define a body-fixed, right-handed Cartesian frame (x_{Bz}, y_{Bz}, z_{Bz}), whose origin is at the center of mass (CM) of Bz, with axes taken parallel to the principal axes of benzene. The z_{Bz} axis is parallel to the C_6 symmetry axis of Bz, the x_{Bz} axis lies along the line bisecting a C–C bond in the molecular plane, and the y_{Bz} axis is defined as: $\mathbf{y}_{Bz} = \mathbf{z}_{Bz} \times \mathbf{x}_{Bz}$. The specific coordinates used below are based on these directions. Second, we introduce a complex-fixed, right-handed Cartesian frame (x, y, z) with its origin at the CM of the Bz–X complex. The z axis points from the CM of Bz to the CM of X. We define the x axis as the projection of x_{Bz} onto the plane

View Article Online
DOI: 10.1039/D5CP04295J

perpendicular to z, followed by normalization; the y axis is then set as: $\mathbf{y} = \mathbf{z} \times \mathbf{x}$.

We defined the position vector, $\mathbf{d}$, pointing from the CM of Bz to the CM of molecule X. The cylindrical coordinates are represented with the pointing vector, as

$$R = d_z,$$
$$\rho = \sqrt{d_x^2 + d_y^2}, \tag{1}$$
$$\phi_{\mathrm{Bz}} = \arctan(d_y/d_x).$$

In addition, the Euler angles $\mathbf{\Omega}_{\mathrm{X}} = (\phi_{\mathrm{X}}, \theta_{\mathrm{X}}, \chi_{\mathrm{X}})$ are invoked to represent the orientation of the principal axis of X with respect to the complex-fixed xyz-axis system. When X=CH_4, the principal axes of X are aligned with the three mutually orthogonal C_2 symmetry axes of the molecule. The Euler angles $\mathbf{\Omega}_{\mathrm{Bz}} = (\phi_{\mathrm{Bz}}, \theta_{\mathrm{Bz}}, \chi_{\mathrm{Bz}})$, are also defined for Bz and the following relations hold:

$$R_{\mathrm{CM}} = R/\cos\theta_{\mathrm{Bz}}, \tag{2}$$
$$\theta_{\mathrm{Bz}} = \arctan(\rho/R), \tag{3}$$

where R_{CM} is the distance between the CMs of Bz and X. The internal coordinates used hereafter are R for the vdW stretch, ρ and ϕ_{Bz} for the vdW bend (or "libration"), and $\mathbf{\Omega}_{\mathrm{X}}$ for the internal rotation of X.

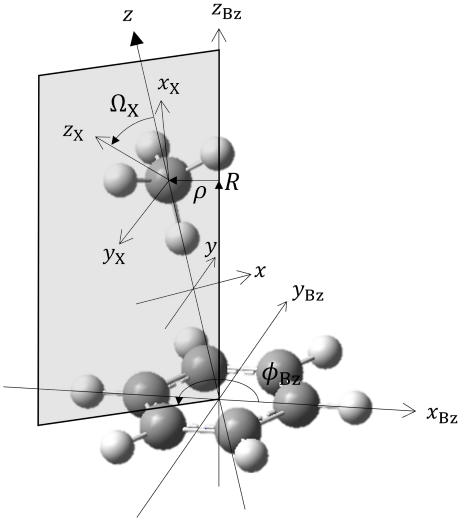

Fig. 1 Coordinate system defined for the Bz–X complex

With the coordinates, Hamiltonian is given by the following formula[38]

$$\hat{H} = \frac{\hat{\mathbf{p}}_d^2}{2\mu} + \sum_{i_{\mathrm{Bz}}} \frac{1}{2I_{i_{\mathrm{Bz}}}} \left[\hat{L}_{i_{\mathrm{Bz}}}^2 + \hat{j}_{i_{\mathrm{Bz}}}^2 + 2\hat{L}_{i_{\mathrm{Bz}}}\hat{j}_{i_{\mathrm{Bz}}}\right] + \sum_{i_{\mathrm{X}}} \left[\frac{1}{2I_{i_{\mathrm{X}}}} \hat{j}_{i_{\mathrm{X}}}^2\right] + V(R, \rho, \phi_{\mathrm{Bz}}, \chi_{\mathrm{Bz}}, \mathbf{\Omega}_{\mathrm{X}}) \tag{4}$$

where $\hat{\mathbf{p}}_d$ is the conjugate momentum of displacement $\mathbf{d}$, μ is the reduced mass corresponding to the displacement $\mathbf{d}$. I and $\hat{j}$ stand for the moment of inertia and the internal rotational angular momentum, respectively, with respect to the principal axes i_{Bz} and i_{X} $(i = x, y, z)$. $\hat{L}_{i_{\mathrm{Bz}}}$ is the x_{Bz}, y_{Bz}, or z_{Bz} component of the end-over-end rotational angular momentum of the complex, defined as $\hat{\mathbf{L}} = \hat{\mathbf{d}} \times \hat{\mathbf{p}}_d$. Then, the total angular momentum is given as: $\hat{\mathbf{J}} = \hat{\mathbf{L}} + \hat{\mathbf{j}}_{\mathrm{Bz}} + \hat{\mathbf{j}}_{\mathrm{X}}$. In the present study, overall rotation of the complex is not considered and thus we set $J = 0$ hereafter.

2.2 General framework of the CSBI potential

The present formalization concentrates the description of low-energy parts of the IPS in the Bz–X system, and we only consider the coordinate space, where X is located above the Bz ring. Interconversion from one side to the other of the Bz ring is not taken into account. Then, the vdW stretch and bend motions are represented as oscillators trapped within potential walls, while the barrier for the internal rotation is so low that full range of the coordinate space have to be covered along the motion.

In the present model, the IPS is represented as an explicit function of the internal coordinates, R, ρ, χ_{Bz}, and $\mathbf{\Omega}_{\mathrm{X}}$, to show the direct correlation of the IPS to the intermolecular motion, unlike the site–site potential utilized in the previous Bz–X studies.[36–39] The IPS is further organized into terms relating to the internal coordinates as,

$$V = V_{\mathrm{S}} + V_{\mathrm{B}} + V_{\mathrm{I}} + V_{\mathrm{SB}} + V_{\mathrm{SI}} + V_{\mathrm{BI}} + V_{\mathrm{SBI}}, \tag{5}$$

where S, B, and I stand for the vdW stretch, bend, and internal rotation, respectively. The first three terms are zero-th order potentials exclusively represented with R, ρ and χ_{Bz}, or $\mathbf{\Omega}_{\mathrm{X}}$. The rest terms in Eq.(5) represent the coupling among stretch, bend, and internal rotation. Each of the basis sets for the wave functions of the zero-th potentials spans a subspace of the overall Hilbert space and the subspaces are connected by the coupling terms.

Each of the terms appearing in Eq.(5) should be expressed in a proper functional form, which obeys the symmetry constraints on the system. In particular, care must be taken for the terms, V_{BI} and V_{SBI}, involving both the bend and the internal rotation, since the vibrational angular momentum of the bend as a 2D oscillator will couple with the 3D internal rotation of the X molecule. To address the issue, we begin with the spherical expansion,[40] where two sets of Euler angles for the internal rotation of constituent molecules are adopted as internal coordinates and thus the angular momentum coupling within the complex is naturally encoded. Contraction of the expansion gives an appropriate form re-expressed with R, ρ, χ_{Bz}, and $\mathbf{\Omega}_{\mathrm{X}}$, as will be shown below.

The spherical expansion is the general formalism to describe the IPS of the binary molecular system,[40,41] and for Bz–X the IPS is given as

$$V(R_{\mathrm{CM}}, \mathbf{\Omega}_{\mathrm{Bz}}, \mathbf{\Omega}_{\mathrm{X}}) = 8\pi^2 \sum_{\substack{L_{\mathrm{Bz}}, L_{\mathrm{X}}, L, \\ M_{\mathrm{Bz}}, M_{\mathrm{X}}, K_{\mathrm{Bz}}, K_{\mathrm{X}}}} (2L+1)^{1/2} v_{L_{\mathrm{Bz}}, L_{\mathrm{X}}, L, M_{\mathrm{Bz}}, M_{\mathrm{X}}, K_{\mathrm{Bz}}, K_{\mathrm{X}}}(R_{\mathrm{CM}}) \times \begin{pmatrix} L_{\mathrm{Bz}} & L_{\mathrm{X}} & L \\ M_{\mathrm{Bz}} & M_{\mathrm{X}} & 0 \end{pmatrix} D^{L_{\mathrm{Bz}}*}_{M_{\mathrm{Bz}}, K_{\mathrm{Bz}}}(\mathbf{\Omega}_{\mathrm{Bz}}) D^{L_{\mathrm{X}}*}_{M_{\mathrm{X}}, K_{\mathrm{X}}}(\mathbf{\Omega}_{\mathrm{X}}), \tag{6}$$

View Article Online
DOI: 10.1039/D5CP04295J

where the expansion coefficients $v_{L_{Bz},L_X,L,M_{Bz},M_X,K_{Bz},K_X}(R_{CM})$ are functions that depend only on the intermolecular distance R_{CM}. $D^L_{M,K}(\mathbf{\Omega})$ stands for Wigner's D-rotational matrix and the large round brackets are 3j-symbol.[43] It is noted that $\phi_{Bz}-\phi_X$ is only independent among the Euler angles and thus the expansion is expressed with the six independent variables.

Because of the large anisotropy for $\mathbf{\Omega}_{Bz}$ due to bulky flat shape of the Bz ring, the convergence of the expansion given in Eq.(6) is quite slow with respect of L_{Bz}, and accordingly L. Then the summation over L_{Bz} and L is formally contracted into a single function, to give the IPS as

$$\begin{aligned} &V(R_{CM},\mathbf{\Omega}_{Bz},\mathbf{\Omega}_X) \\ &= \sum_M \sum_{L_X,K_X} \mathrm{e}^{-\mathrm{i}M\phi_{Bz}} f^{L_X}_{M,K_X}(R_{CM},\theta_{Bz},\chi_{Bz}) D^{L_X*}_{-M,K_X}(\mathbf{\Omega}_X), \end{aligned} \tag{7}$$

with

$$\begin{aligned} &f^{L_X}_{M,K_X}(R_{CM},\theta_{Bz},\chi_{Bz}) \\ &= 8\pi^2 \sum_{L,L_{Bz},K_{Bz}} (2L+1)^{1/2} v_{L_{Bz},L_X,L,M,-M,K_{Bz},K_X}(R_{CM}) \\ &\times \begin{pmatrix} L_{Bz} & L_X & L \\ M & -M & 0 \end{pmatrix} d^{L_{Bz}*}_{M,K_{Bz}}(\theta_{Bz}) \mathrm{e}^{-\mathrm{i}K_{Bz}\chi_{Bz}}. \end{aligned} \tag{8}$$

with $d^L_{M,K}$ being the Wigner's small d-matrix.[43] In recasting Eq.(6) into Eqs.(7) and (8), we utilized the non-vanishing condition for 3j-symbol, i.e., $M_{Bz}=-M_X\equiv M$.

The variables R_{CM} and θ_{Bz}, appearing in Eqs.(7) and (8) are related to R and ρ, as given in Eqs.(2) and (3). Then, the IPS in Eq.(7) is re-expressed with an appropriate coordinate system as

$$\begin{aligned} &V(R,\rho,\phi_{Bz},\chi_{Bz},\mathbf{\Omega}_X) \\ &= \sum_M \sum_{L_X,K_X} \mathrm{e}^{-\mathrm{i}M\phi_{Bz}} f^{L_X}_{M,K_X}(R,\rho,\chi_{Bz}) D^{L_X*}_{-M,K_X}(\mathbf{\Omega}_X). \end{aligned} \tag{9}$$

Apparent redundancy in the variables is due to the correlation between ϕ_{Bz} and ϕ_X, as mentioned before. Based on the general formula given in Eq.(9), the CSBI potential for a specific Bz–X system will be constructed in a form given in Eq.(5) by suitable parameterization of $f^{L_X}_{M,K_X}$.

2.3 The CSBI potential of Bz–methane

In this section, we will determine a specific functional form for the IPS of Bz–methane by incorporating the symmetry of the system into the CSBI framework discussed in the previous section.

First, the term with $L_X=0$ in Eq.(9) is independent of $\mathbf{\Omega}_X$ since the D-matrix with rank 0 is simply a scalar. Then,

$$f^0_{0,0}(R,\rho,\chi_{Bz}) = V_S + V_B + V_{SB}. \tag{10}$$

Here we follow the functional forms adopted in the previous studies on Bz–Ar,[28,29] i.e., the Morse type potential for the zero-th order potential for the stretch as

$$V_S(R) = k_{zz}\{1-\exp[-a(R-R_e)]\}^2, \tag{11}$$

the isotropic 2D harmonic potential for the zero-th order potential for the bend as

$$V_B(\rho) = k_{xx}\rho^2, \tag{12}$$

and the coupling term between the stretch and bend as

$$V_{SB}(R,\rho) = k_{xxz}\rho^2\{1-\exp[-a(R-R_e)]\}, \tag{13}$$

where R_e is the value for R at the potential minimum, and k_{zz}, k_{xx}, and k_{xxz} are force constants. It is noted that the potential terms, V_B and V_{SB}, are set independent of χ_{Bz}. Due to the 6-fold rotational symmetry of Bz, the potential may possess terms proportional to $\cos(6\chi_{Bz})$, $\cos(12\chi_{Bz})$, …, but their contribution is regarded marginal. Thus, the χ_{Bz}-dependence in the potential is not considered throughout the following discussion, i.e., $f^{L_X}_{0,K_X}(R,\rho,\chi_{Bz}) \to f^{L_X}_{0,K_X}(R,\rho)$.

The term $f^{L_X}_{M,K_X}(R,\rho)$ with $L_X>0$ and $M=0$ is pertinent to the internal rotational potential. We assumed that anisotropy of the internal rotational potential of methane is so small that it can be described with lower order terms of rotational matrix expansion. Considering T_d symmetry of methane, the lowest terms are expressed as a symmetry-adapted linear combination of the rotational matrices with $L_X=3$ and 4, as follows.[44–49]

$$\begin{aligned} T^3_0(\mathbf{\Omega}_X) &= D^{3*}_{0,2}(\mathbf{\Omega}_X) + D^{3*}_{0,-2}(\mathbf{\Omega}_X) \\ &= C^3_2(\theta_X,\chi_X) + C^3_{-2}(\theta_X,\chi_X) \end{aligned} \tag{14}$$

$$\begin{aligned} T^4_0(\mathbf{\Omega}_X) &= \sqrt{14}D^{4*}_{0,0}(\mathbf{\Omega}_X) - \sqrt{5}\left[D^{4*}_{0,4}(\mathbf{\Omega}_X) + D^{4*}_{0,-4}(\mathbf{\Omega}_X)\right] \\ &= \sqrt{14}C^4_0(\theta_X,\chi_X) - \sqrt{5}\left[C^4_4(\theta_X,\chi_X) + C^4_{-4}(\theta_X,\chi_X)\right] \end{aligned} \tag{15}$$

where C^p_q is renormalized spherical harmonics. When the T^3_0 and T^4_0 terms are only considered, it is commonly referred to as the hindered rotor model: $V_{3D}=V^3_0T^3_0(\mathbf{\Omega}_X)+V^4_0T^4_0(\mathbf{\Omega}_X)$, where V^3_0 and V^4_0 are potential constants.[44–49] The 3D hindered rotor model is extended in the present 6D model to include terms representing the coupling between $\mathbf{\Omega}_X$ and R or ρ. Specifically, we applied a Taylor expansion with respect to R and ρ, as

$$V(R,\rho,\mathbf{\Omega}_X) = f^3_0(R,\rho)T^3_0(\mathbf{\Omega}_X) + f^4_0(R,\rho)T^4_0(\mathbf{\Omega}_X) \tag{16}$$

with

$$f^{L_X}_0(R,\rho) = V^{L_X}_0 + \partial_R V^{L_X}_0 (R-R_e) + \partial^2_R V^{L_X}_0 (R-R_e)^2 + \partial^2_\rho V^{L_X}_0 \rho^2 \tag{17}$$

for $L_X=3$ and 4. Here, $V^{L_X}_0 = V^{L_X}_0(R_e,\rho_e)$, $\partial_R V^{L_X}_0$, $\partial^2_R V^{L_X}_0$, and $\partial^2_\rho V^{L_X}_0$ are potential constants. The potential in Eq.(16) is recast into the terms appearing in Eq.(5) as

$$V(R,\rho,\mathbf{\Omega}_X) = V_I + V_{SI} + V_{BI_1}, \tag{18}$$

with

$$V_I(\mathbf{\Omega}_X) = V^3_0T^3_0(\mathbf{\Omega}_X) + V^4_0T^4_0(\mathbf{\Omega}_X), \tag{19}$$

View Article Online
DOI: 10.1039/D5CP04295J

being the zero-th order potential for the internal rotation,

$$V_{\mathrm{SI}}(R,\mathbf{\Omega}_{\mathrm{X}}) = \left[\partial_R V_0^3 T_0^3(\mathbf{\Omega}_{\mathrm{X}}) + \partial_R V_0^4 T_0^4(\mathbf{\Omega}_{\mathrm{X}})\right](R-R_{\mathrm{e}}) + \left[\partial_R^2 V_0^3 T_0^3(\mathbf{\Omega}_{\mathrm{X}}) + \partial_R^2 V_0^4 T_0^4(\mathbf{\Omega}_{\mathrm{X}})\right](R-R_{\mathrm{e}})^2, \quad (20)$$

being the coupling terms between the stretch and internal rotation, and

$$V_{\mathrm{BI}_1}(\rho,\mathbf{\Omega}_{\mathrm{X}}) = \left[\partial_\rho^2 V_0^3 T_0^3(\mathbf{\Omega}_{\mathrm{X}}) + \partial_\rho^2 V_0^4 T_0^4(\mathbf{\Omega}_{\mathrm{X}})\right]\rho^2, \quad (21)$$

being a part of the coupling terms between the bend and internal rotation.

In addition to V_{BI_1} given in Eq.(21), ϕ_{Bz}-dependent terms, i.e. with $M \neq 0$, should be invoked into V_{BI}. Judging from Eq.(6), the terms are expressed with $D^{L_{\mathrm{Bz}}*}_{M,K_{\mathrm{Bz}}}(\mathbf{\Omega}_{\mathrm{Bz}})D^{L_{\mathrm{X}}*}_{-M,K_{\mathrm{X}}}(\mathbf{\Omega}_{\mathrm{X}})$. In the present study, the overall rotation of the complex is not considered and thus the scalar ($L = 0$) terms in Eq. (6) are only retained with $L_{\mathrm{Bz}} = L_{\mathrm{X}} = 3$ as the lowest-order contribution. To consider only the lowest-order azimuthal dependence, we also restrict our consideration to the $M = \pm 1$ components. In addition, we set $K_{\mathrm{Bz}} = 0$ because the potential is assumed independent of χ_{Bz}; hence all Fourier components with $K_{\mathrm{Bz}} \neq 0$ vanish. Then, the lowest terms fulfilling the T_d symmetry of methane are given as

$$V_{\mathrm{BI}_2} = V_1^3\left[C_1^3(\theta_{\mathrm{Bz}},\phi_{\mathrm{Bz}})T_{-1}^3(\mathbf{\Omega}_{\mathrm{X}}) + C_{-1}^3(\theta_{\mathrm{Bz}},\phi_{\mathrm{Bz}})T_1^3(\mathbf{\Omega}_{\mathrm{X}})\right] \quad (22)$$

with

$$T_{\pm 1}^3(\mathbf{\Omega}_{\mathrm{X}}) = D_{\pm 1,2}^{3*}(\mathbf{\Omega}_{\mathrm{X}}) + D_{\pm 1,-2}^{3*}(\mathbf{\Omega}_{\mathrm{X}}) \quad (23)$$

where V_1^3 is a potential constant. It is noted that the terms given in Eq. (22) induce the coupling between the angular momenta of the 2D bend (libration) and the 3D internal rotation. The sum of V_{BI_1} given in Eq. (21) and V_{BI_2} given in Eq. (22) results in the coupling between the bend and the internal rotation, V_{BI}.

The *ab initio* computation on the IPS, to be described just below, has shown that the angular momentum coupling depends on the intermolecular distance R: the coupling decreases as R becomes longer. Consequently, we introduced the terms that empirically incorporate the decaying factor of R^{-6}, as

$$V_{\mathrm{SBI}} = V_{1,R}^3\left[C_1^3(\theta_{\mathrm{Bz}},\phi_{\mathrm{Bz}})T_{-1}^3(\mathbf{\Omega}_{\mathrm{X}}) + C_{-1}^3(\theta_{\mathrm{Bz}},\phi_{\mathrm{Bz}})T_1^3(\mathbf{\Omega}_{\mathrm{X}})\right]R^{-6} \quad (24)$$

where $V_{1,R}^3$ is a potential constant.

3 Computational Details

3.1 Construction of the potential

In the *ab initio* IPS calculation, we used Gaussian 16 program[50] with the coupled cluster singles and doubles including connected triples model[51,52] in conjunction with augmented correlation consistent polarized valence triple zeta basissets[53,54] [CCSD(T)/aug-cc-pVTZ] for energy calculation and determination of molecular structure.

Whether the present level of theory is sufficiently accurate for the problem under study must be carefully evaluated. A benchmark study on hydrocarbon systems has assessed the accuracy of conventional CCSD(T) as well as explicitly correlated CCSD(T)-F12 approaches.[55] In that work, the CCSD(T)-F12 method was shown to converge rapidly and reliably toward the CCSD(T)/CBS limit, with deviations of only 0.002–0.004 kcal mol^{-1} (~ 0.70–1.40 cm^{-1}). At the CCSD(T)/aug-cc-pVTZ level of theory, the remaining error was at most 0.016 kcal mol^{-1} (~ 5.6 cm^{-1}), which corresponds to only a few percent of the total binding energy of approximately 1.4 kcal mol^{-1}. In addition, Oviedo *et al.*[56] investigated static polarizabilities and hyperpolarizabilities of π-conjugated systems and provided new benchmark data at both the CCSD(T) and CCSD(T)-F12 levels of theory. They demonstrated that CCSD(T)-F12 reproduces the conventional CCSD(T) results for these response properties with only very small differences, indicating that both approaches may be regarded as benchmark quality. Although CCSD(T)-F12 could further improve the calculated results, the conventional CCSD(T) approach already should provide a reasonable level of accuracy for the present problem.

Single-point energy calculations were performed for the molecular orientation grids shown in Table 1. Owing to the D_{6h} symmetry of the benzene ring and the T_d symmetry of methane, the number of unique grid points can be significantly reduced. In these calculations, both the monomer units were frozen at their respective equilibrium geometries. The most stable structures of each molecule were individually determined by performing optimization calculation at the CCSD(T)/aug-cc-pVTZ level of theory using Gaussian 16 with the Opt=Normal option, as shown in Table 2. Here the self-consistent field (SCF) procedure was converged to a root-mean-square (RMS) change in the density matrix of 1.0×10^{-8}, a maximum density change of 1.0×10^{-6}, and an energy change of 1.0×10^{-6} E_h. Geometry optimization was considered converged when the maximum and RMS Cartesian gradients were smaller than 4.5×10^{-4} and 3.0×10^{-4} E_h Bohr^{-1}, respectively. In addition, the maximum and RMS Cartesian displacements were required to be smaller than 1.8×10^{-3} and 1.2×10^{-3} Bohr, respectively. In this study, the benzene molecule was further simplified as an ideal circular disk rather than treating its full D_{6h} structure, which allowed an additional reduction of redundant configurations. Equivalent orientations related by symmetry operations (e.g., rotation around the benzene C_6 axis and permutation of the four C–H bonds of methane) were not explicitly calculated.

For the internal rotation, we set the following three grids in addition to the equidistant grids shown in Table 1: (1) the "monodentate" conformation, where a C–H bond of methane points towards the center of the Bz ring with $(\theta_{\mathrm{X}},\chi_{\mathrm{X}}) = (54.7°, 0°)$, (2) the "bidentate" conformation, where a rige connecting two H atoms of methane faces to the Bz ring with $(\theta_{\mathrm{X}},\chi_{\mathrm{X}}) = (90°, 45°)$, and (3) the "tridentate" conformation, where a triangle face of the methane tetrahedron points towards the Bz ring as $(\theta_{\mathrm{X}},\chi_{\mathrm{X}}) = (54.7°, 90°)$. Due to the T_d symmetry of methane, these three sets of the angles correspond to representatives of four equivalent monodentate, six equivalent bidentate, and four equivalent tridentate conformations, respectively. Only one representative geometry from

View Article Online
DOI: 10.1039/D5CP04295J

each set was considered in the *ab initio* calculation.

The results of the single-point energy calculation for the 525 grids are processed to the least-squares regression with the CSBI potential described in the preceding section.

Table 1 Grids for single-point energy calculation

Variables	Grids
R /Å	3.40, 3.55, 3.70, 3.85, 4.00
ρ /Å	0.0, 0.3, 0.6
ϕ_{Bz} /°	0, 120, 240
θ_{X} /°	30, 60, 90
χ_{X} /°	0, 30, 60, 90

Table 2 Geometrical parameters determined by monomer optimization

Molecule	Parameter	Value
CH_4	r_{CH} /Å	1.089912
Bz	r_{CC} /Å	1.397992
Bz	r_{CH} /Å	1.083921

3.2 Calculation of the intermolecular vibrational levels

Matrix elements for The Hamiltonian given in Eq.(4) [with the potential represented as Eq. (5) with each term given in Eqs.(11, 12, 13, 19, 20, 21, 22, 24)] are evaluated by using the stretch-bend-internal-rotation basis set, which is represented as a direct product, $\{|n_0\rangle|n_+,n_-\rangle|j_{\mathrm{X}},k_{\mathrm{X}},m_{\mathrm{X}}\rangle\}$. Here $\{|n_0\rangle\}$ is a one-dimensional harmonic oscillator basis on R for the stretching mode, $\{|n_+,n_-\rangle\}$ is a two-dimensional harmonic oscillator basis on ρ and ϕ_{Bz} for the bending mode, and $\{|j_{\mathrm{X}},k_{\mathrm{X}},m_{\mathrm{X}}\rangle\}$ is a symmetric-top rotor basis on $\mathbf{\Omega}_{\mathrm{X}} = (\phi_{\mathrm{X}},\theta_{\mathrm{X}},\chi_{\mathrm{X}})$ for the internal rotation of X (= CH_4 in this case). The bending basis $\{|n_+,n_-\rangle\}$ correlates to the conventional two-dimensional oscillator basis $\{|v,l\rangle\}$ as

$$\begin{aligned} v &= n_+ + n_-, \\ l &= n_+ - n_-. \end{aligned} \tag{25}$$

The discrete variable representation (DVR) was employed for the stretching mode $\{|n_0\rangle\}$, to calculate matrix elements of the Morse potential. The kinetic and potential-energy matrix elements were evaluated analytically using creation and annihilation (ladder) operators, $\hat{A}^\dagger$ and $\hat{A}$.[57,58] The coordinate and momentum operators are expressed with $\hat{A}^\dagger$ and $\hat{A}$ as

$$\hat{d}_i = \sqrt{\frac{\hbar}{2\mu_i\omega_i}}(\hat{A}_i^\dagger + \hat{A}_i) \qquad (i = x,y,z), \tag{26}$$

$$\hat{p}_i = \mathrm{i}\sqrt{\frac{\mu_i\hbar\omega_i}{2}}(\hat{A}_i^\dagger - \hat{A}_i) \qquad (i = x,y,z). \tag{27}$$

We further define

$$\begin{aligned} \hat{A}_0^\dagger &= \hat{A}_z^\dagger, & \hat{A}_0 &= \hat{A}_z \\ \hat{A}_\pm^\dagger &= \frac{1}{\sqrt{2}}(\hat{A}_x^\dagger \pm \mathrm{i}\hat{A}_y^\dagger), & \hat{A}_\pm &= \frac{1}{\sqrt{2}}(\hat{A}_x \mp \mathrm{i}\hat{A}_y). \end{aligned} \tag{28}$$

The reduced masses for the stretch and bend[59] are defined as

$$\frac{1}{\mu_z} = \frac{1}{\mu_{\mathrm{S}}} = \frac{1}{\mu}, \tag{29}$$

$$\frac{1}{\mu_x} = \frac{1}{\mu_y} = \frac{1}{\mu_{\mathrm{B}}} = \frac{1}{\mu} + \frac{R_{\mathrm{e}}^2}{I_x}. \tag{30}$$

The fundamental harmonic frequencies are given as

$$\omega_z = \omega_{\mathrm{S}} = \sqrt{\frac{2k_{zz}a^2}{\mu_{\mathrm{S}}}}, \tag{31}$$

$$\omega_x = \omega_y = \omega_{\mathrm{B}} = \sqrt{\frac{2k_{xx}}{\mu_{\mathrm{B}}}}. \tag{32}$$

The matrix elements of the ladder operators are given as

$$\langle n_q''|\hat{A}_q^\dagger|n_q'\rangle = \sqrt{n_q'+1}\,\delta_{n_i'',n_q'+1} \qquad (q = 0,\pm), \tag{33}$$

$$\langle n_q''|\hat{A}_q|n_q'\rangle = \sqrt{n_q'}\,\delta_{n_q'',n_q'-1} \qquad (q = 0,\pm). \tag{34}$$

The angular momentum operator is expressed as

$$\hat{L}_{i_{\mathrm{Bz}}} = \tfrac{1}{2}\,\varepsilon_{ijk}\big(\hat{d}_j\hat{p}_k - \hat{p}_k\hat{d}_j\big), \qquad i,j,k \in \{x,y,z\}, \tag{35}$$

where ε_{ijk} is the Levi-Civita symbol. The spherical harmonic component relevant to the interaction terms given in Eqs.(22) and (24) is written as

$$C_{\pm1}^3(\theta_{\mathrm{Bz}},\phi_{\mathrm{Bz}}) = \frac{1}{8}\sqrt{\frac{21}{\pi}}\,\frac{(\hat{d}_x \pm i\hat{d}_y)(5\hat{d}_z^2 - |\hat{\mathbf{d}}|^2)}{|\hat{\mathbf{d}}|^3}. \tag{36}$$

For the internal rotation, matrix elements of the angular-momentum components were evaluated by recasting them into the ladder operators[43] defined as

$$\hat{j}_+ = \hat{j}_x + i\hat{j}_y, \tag{37}$$

$$\hat{j}_- = \hat{j}_x - i\hat{j}_y. \tag{38}$$

The matrix elements for the potential terms in Eqs.(19, 20, 21, 22) were evaluated by using the the standard 3-j symbol expression for the Wigner D-matrix:[43]:

$$\begin{aligned} &\left\langle j_{\mathrm{X}}'',k_{\mathrm{X}}'',m_{\mathrm{X}}''\middle|D_{m,k}^{j}\middle|j_{\mathrm{X}}',k_{\mathrm{X}}',m_{\mathrm{X}}'\right\rangle \\ &= (-1)^{m_{\mathrm{X}}''-k_{\mathrm{X}}''}\sqrt{(2j_{\mathrm{X}}'+1)(2j_{\mathrm{X}}''+1)}\begin{pmatrix} j_{\mathrm{X}}'' & j & j_{\mathrm{X}}' \\ -k_{\mathrm{X}}'' & k & k_{\mathrm{X}}' \end{pmatrix}\begin{pmatrix} j_{\mathrm{X}}'' & j & j_{\mathrm{X}}' \\ -m_{\mathrm{X}}'' & m & m_{\mathrm{X}}' \end{pmatrix}. \end{aligned} \tag{39}$$

To evaluate the kinetic energy terms in the Hamiltonian given in Eq. (4), we adopted rotational constants of the monomers experimentally determined by high-resolution spectroscopy,[60,61] as listed in Table 3. This choice would be more appropriate than adopting the calculated equilibrium values, if we would compare the calculated intermolecular vibrational energy levels with experimental observation, since the moments of inertia and the corresponding rotational constants are affected by zero-point vibrational averaging over the intramolecular modes.

View Article Online
DOI: 10.1039/D5CP04295J

Table 3 Molecular parameters used for the calculation of energy eigenstates

Molecule	Parameter	Value
CH_4	B /cm^{-1}	5.241 036[a]
Bz	B /cm^{-1}	0.189 762[b]
Bz	C /cm^{-1}	0.094 881[b]
–	$\mu/10^{-26}$ kg	2.210 88

[a]From ref. ([60]). [b]From ref. ([61]).

Eigenvalues and eigenvectors for the intermolecular vibrational levels of Bz–methane were derived by diagonalizing the Hamiltonian matrices. Because the system is invariant under rotations around the z axis, the projection of the total angular momentum onto this axis is conserved. Accordingly, $m = m_X + l = m_X + (n_+ - n_-)$ is a good quantum number, and the Hamiltonian is diagonal with respect to m. The diagonalization of the real symmetric Hamiltonian matrix was performed using the DSYEVD routine from the Linear Algebra PACKage (LAPACK) version 3.10.1.[62] We included the basis functions with the quantum numbers up to $n_{0,\max} = 8$, $n_{+,\max} = n_{-,\max} = 6$, and $j_{X,\max} = k_{X,\max} = 7$. With these basis limits, the matrix dimension was approximately 2.0×10^4 for each quantum number m_X. The computed eigenvalues converged within 0.3 cm^{-1}, covering energy levels from the ground state up to 65 cm^{-1}. It is noted that each of the intermolecular vibrational states belongs to an irreducible representation, A, E, or F, due to T_d symmetry of methane. Symmetry specification was conducted by examining degeneracy and composition of the states.

4 Results and Discussion

4.1 Determined potential parameters

The parameters in the CSBI potential of Bz–methane thus obtained are listed in Table 4. The standard deviation of the least-squares fit is 9.3 cm^{-1}.

Table 4 Parameters of the CSBI potential obtained for Bz–methane

Parameter	Value
R_e / Å	3.631
k_{zz} / cm^{-1}	615.484
a / Å^{-1}	1.450
k_{xx} / cm^{-1}Å^{-2}	145.182
k_{xxz} / cm^{-1}Å^{-3}	−183.035
V_0^3 / cm^{-1}	−50.062
V_0^4 / cm^{-1}	3.663
$\partial_R V_0^3$ / cm^{-1}Å^{-1}	−191.741
$\partial_R V_0^4$ / cm^{-1}Å^{-1}	14.143
$\partial_R^2 V_0^3$ / cm^{-1}Å^{-2}	322.193
$\partial_R^2 V_0^4$ / cm^{-1}Å^{-2}	−20.267
$\partial_\rho^2 V_0^3$ / cm^{-1}Å^{-2}	44.282
$\partial_\rho^2 V_0^4$ / cm^{-1}Å^{-2}	−1.037
$V_{\pm1}^3$ / cm^{-1}	477.340
$V_{\pm1,R}^3$ / 10^6 cm^{-1}Å^6	−2.173 12

The most notable point in Table 4 is that the absolute values of V_0^3 is one order of magnitude larger than that of V_0^4. The predominance of V_0^3 with the positive sign is a clear signature that the monodentate conformation is the most stable geometry in Bz–methane. The value of the intermolecular distance R at the global minima is 3.712 Å with $\rho = 0$. The bidentate conformation is a saddle point on the internal-rotation potential. It is higher than the potential minima by 57.267 cm^{-1}, when the CM of methane is in its most stable position ($R = 3.636$ Å and $\rho = 0$). The tridentate conformation is positioned above the monodentate configuration by 105.648 cm^{-1} with $R = 3.558$ Å and $\rho = 0$.

In the present CSBI model, the full coordinate space for the total Hamiltonian given in Eq.(4) is constructed with the three subspaces for the internal motions, i.e., stretch, bend, and internal rotation. The off-diagonal potential terms, i.e., V_{SB}, V_{SI}, V_{BI}, and V_{SBI}, connect the subspaces. Here we address an intuitive energy estimation among the coordinate space. The vibrational frequencies, $\omega_S = 81.06$ cm^{-1} and $\omega_B = 46.92$ cm^{-1}, are taken as the energies that characterize the stretch and bend subspaces, respectively. Regarding a characteristic energy of the internal rotation, we can take the barrier height, i.e., the energy difference between the minima and the saddle point ($w_I = 114.24$ cm^{-1}).

Estimates of typical energies for the coupling between the subspaces can be done as follows. Among the parameters appearing in the off-diagonal terms listed in Table 4, $\partial_R V_0^3$, $\partial_R V_0^4$, $\partial_R^2 V_0^3$, and $\partial_R^2 V_0^4$ are the coefficients appeared in the Taylor expansion with R. Then we adopt the full width at half maximum (FWHM) of the stretch ground-state wave function, δR, as a typical value for $(R - R_e)$. It is calculated to be ~ 0.42 Å. By multiplying the parameters with δR or $(\delta R)^2$, the coupling energies are evaluated. Similarly, the coupling between the bend and the internal rotation is estimated by multiplying $\partial_\rho^2 V_0^3$ and $\partial_\rho^2 V_0^4$ with $(\delta\rho)^2$, where $\delta\rho$ is the FWHM for the bend and its value is ~ 0.95 Å. For the stretch–bend coupling, the coupling energy was estimated by multiplying k_{xxz} with $(\delta R)^2\delta\rho$. For the angular momentum coupling, the parameters $V_{\pm1}^3$ and $V_{\pm1,R}^3$ are scaled by a factor of $C_{\pm1}^3(\delta\theta_{Bz}, 0) \sim 0.2$, with $\delta\theta_{Bz} = \delta\rho/R_e$. The $V_{\pm1,R}^3$ parameter is further factored by R_e^{-6}. The results are summarized in Table 5.

Table 5 Coupling energies estimated from the parameters listed in Table 4

Parameter	Corresponding energy / cm^{-1}
k_{xxz}	−50
$\partial_R V_0^3$	−80
$\partial_R V_0^4$	6
$\partial_R^2 V_0^3$	60
$\partial_R^2 V_0^4$	−3
$\partial_\rho^2 V_0^3$	40
$\partial_\rho^2 V_0^4$	−1
$V_{\pm1}^3$	110
$V_{\pm1,R}^3$	−190

One of the notable points of Table 5 is that several coupling terms are in the same energy range as ω_S, ω_B, or w_I. This manifests substantial coupling among the internal coordinates of the stretch, bend, and internal rotation. Thus, reduced dimensional analysis is totally inadequate to describe the intermolecular vi-

View Article Online
DOI: 10.1039/D5CP04295J

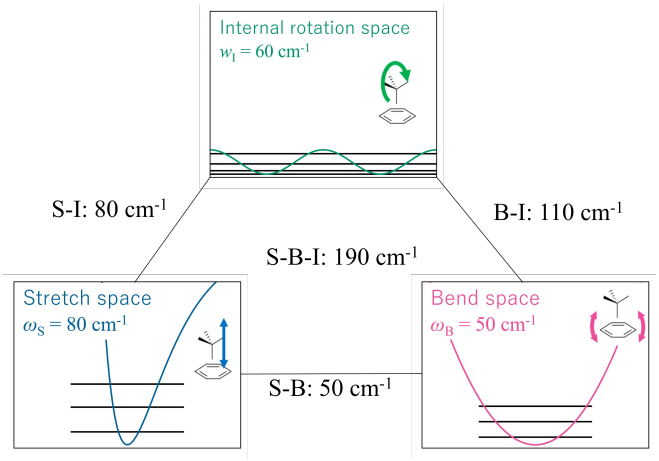

Fig. 2 Schematic representation of the characteristic energies among the coordinate subspaces in the Bz–methane system

bration of Bz–methane. In particular, $V^3_{\pm1}$ and $V^3_{\pm1,R}$, to represent the angular momentum coupling between the internal rotation and the bend, dominate others. This feature gives a significant impact on the IPS, as discussed in the following. Figure 2 represents schematically the mode-coupling characteristics in the IPS of Bz–methane. This diagram symbolizes the motivation to build the CSBI model as given in Eq. 5.

The coupling between the stretch, bend, and internal rotation in the IPS can be visualized when we examine perspective 2D cross sections out of the 6D IPS. In particular, we focus on the cross sections that highlight the contribution of the three dominant potential parameter; $V^3_{\pm1}$, $V^3_{\pm1,R}$, and $\partial_R V^3_0$. As shown in Figs. 3 and 4, we can gain an intuitive understanding on the coupling effects by comparing the cross sections of the IPSs with and without the specific coupling terms of interest.

Figure 3 shows 2D plots of the IPS along the bend (ρ) and internal-rotation (χ_X) coordinates. The rest coordinates are set to the values at the equilibrium position. The left panel shows the complete IPS while the right panel shows the IPS with $V^3_{\pm1}$ and $V^3_{\pm1,R}$ set zero. The difference between the two plots instructs the contribution of the angular momentum coupling terms. While the minimum energy path (MEP) is a straight line in the right panel, it becomes curved in the left panel, to show the two coordinates are not separable. In a classical view point, the bend and the internal rotation are interlocked to each other, as a result of the angular momentum coupling between the two modes. Another notable point is that the coupling results in the reduction of the curvature along the MEP: the blue region in the left panel is extended along the ρ direction. If we take an effective 1D model for the bend, its vibrational frequency is reduced due to the coupling with the internal rotation.

Figure 4 shows 2D cross sections of the IPS along R and χ_X, to show the coupling between the stretch and the internal rotation. The left panel represents the complete IPS while the right shows the IPS with $\partial_R V^3_0 = \partial_R V^4_0 = \partial^2_R V^3_0 = \partial^2_R V^4_0 = 0$. In these plots, the minimum at $\chi_X = 180°$ corresponds to the monodentate conformation where one of the methane C–H bonds points to the CM of Bz, while the saddle points at $\chi_X = 90,\ 270°$ correspond to the tridentate conformation where one of the faces of the methane tetrahedron points to the Bz plane. In the right panel, the MEP is depicted as a straight line, indicating that the methane unit rotates without changing the intermolecular distance. In the left panel, the saddle points are allocated at the positions with smaller value of R than at the global minimum. This figure visualizes the intermolecular distance depending on the orientation of methane along the MEP. The difference in R between the two positions is ~ 0.17 Å.

Figure 5 shows a schematic representation of the motion of methane along the MEP, indicated in the left panel of Fig. 3. At the equilibrium geometry with $\rho = 0$, one of the C–H bonds of methane points to the CM of Bz; it lies along the intermolecular z axis. However, as the bend angle ρ becomes larger, the C–H bond becomes off from the intermolecular axis due to the coupling between the bend and internal rotation. This is in contrast to the case without the angular momentum coupling, i.e., $V^3_{\pm1} = V^3_{\pm1,R} = 0$, where the C–H bond always points to the CM of Bz. As shown in Fig. 5, the closest H atom tends to remain on the center of the Bz ring in the complete IPS, as the atom looks fit to the central dent of the π electron cloud on the Bz ring.

Figure 6 represents schematically the motion of methane along the MEP, indicated in the left panel of Fig. 4. The shrinkage of the intermolecular distance as the methane rotates away from the monodentate conformation is naturally rationalized by the fact that the repulsive part of the intermolecular interaction in Bz–methane is mostly scaled with the distance of the nearest H atom(s) from the Bz plane. Thus, the optimum R for the tridentate conformation is shorter than that for the monodentate one. Such IPS couplings, visualized in Figs. 5 and 6 cause substantial complication in the energy-level structure for the intermolecular vibration in Bz–methane, as discussed below.

4.2 Eigenstate analysis

Energy levels obtained by diagonalizing the full Hamiltonian matrices constructed on the CSBI model are graphically represented in Fig. 7. In this energy-level diagram, the results with all the potential terms included (right part) are correlated with those excluding the effects from the mode coupling by setting $V_{SB} = V_{SI} = V_{BI} = V_{SBI} = 0$ (middle) and those for free internal rotation of methane by further setting $V_I = 0$ (left). In the case of free internal rotation, the energy-level structure is just the same as that of methane monomer rotation, with addition of vdW stretch and bend levels. By including the internal-rotation potential, each of j levels is split into $(j+1)$ multiplets with $m = 0, \pm1, \pm2, ..., \pm j$ as the internal rotation is hindered by the anisotropic potential. When the full potential is considered, the energy levels are substantially shifted from the case for the hindered internal-rotation model by the effects of mode coupling. Since the inclusion of the coupling terms results in flattening of the potential (as seen in Fig. 3), majority of the levels are stabilized by the mode coupling. Thus, the state density of the fully coupled levels (right) is higher than that without mode coupling (middle). It is noted that levels with A, E, and F symmetry couple with different nuclear spin states, between which interconversion is quite slow in adiabatic expan-

View Article Online
DOI: 10.1039/D5CP04295J

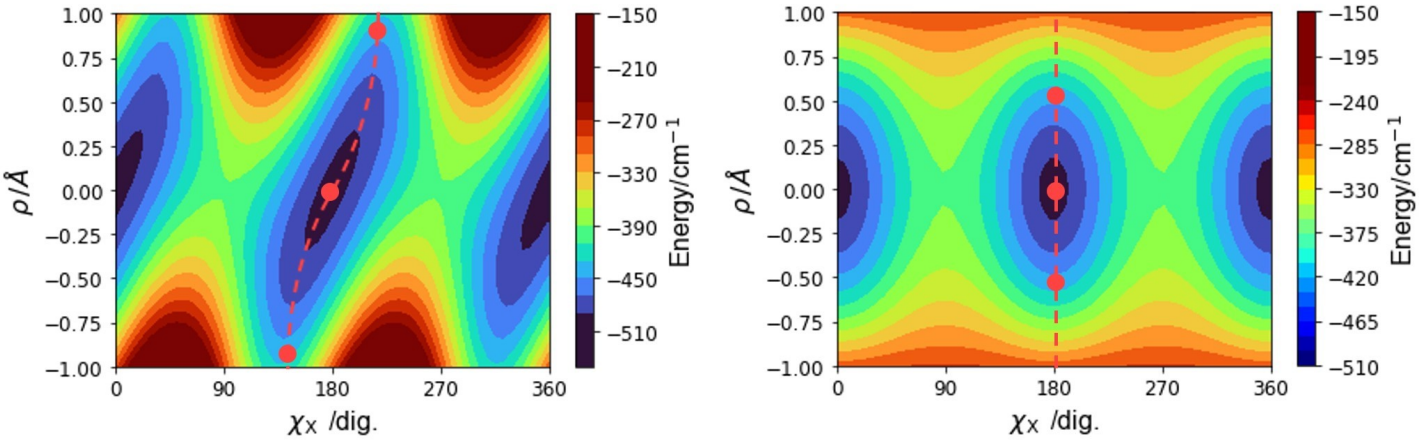

Fig. 3 2D cross section of the IPS along the bend (ρ) and internal-rotation (χ_X) coordinates, with $R = R_e$, $\phi_{Bz} = 0$, $\phi_X = 0$, and $\theta_X = 54.7°$. Left: the complete IPS with the fitted parameters listed in Table 4. Right: the IPS with $V^3_{\pm1} = V^3_{\pm1,R} = 0$. The dashed lines represent the minimum energy path on the cross sections. The red dot at $\rho = 0$ corresponds to the minimum, while the other two are taken at arbitrary positions along the path.

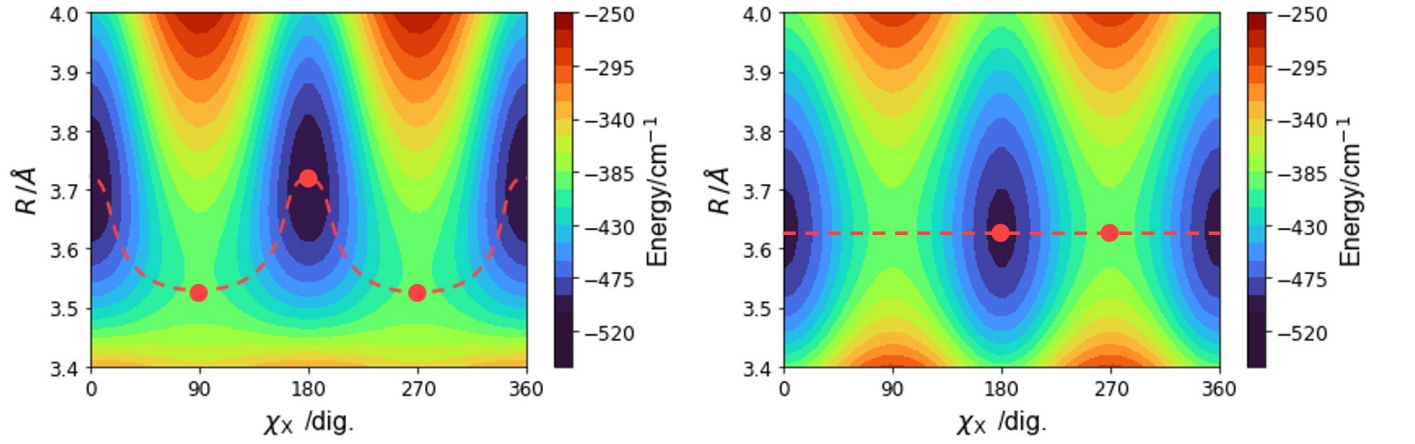

Fig. 4 2D cross section of the IPS along the stretch (R) and internal-rotation (χ_X) coordinates, with $\rho = 0$, $\phi_{Bz} = 0$, $\phi_X = 0$, and $\theta_X = 54.7°$. Left: the complete IPS with the fitted parameters listed in Table 4. Right: the IPS with $\partial_R V^3_0 = \partial_R V^4_0 = \partial^2_R V^3_0 = \partial^2_R V^4_0 = 0$. The dashed lines represent the minimum energy path on the cross sections, and the red dots indicate the minimum and saddle points.

View Article Online
DOI: 10.1039/D5CP04295J

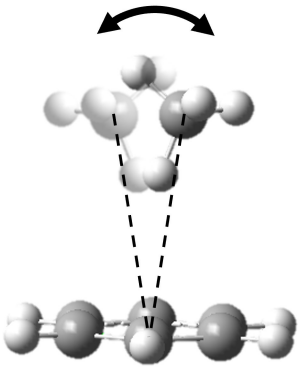

Fig. 5 Schematic representation of the bending motion along the minimum energy path, indicated in the left panel of Fig. 3: ρ is set to be 0.5 Å. The dashed lines connect the CMs of the two monomer unit; due to the coupling, the C–H bond is displaced away from pointing to the center of the Bz ring.

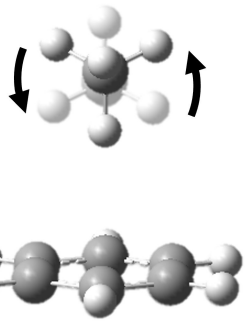

Fig. 6 Schematic representation of the internal rotational motion of methane along the minimum energy path, indicated in the left panel of Fig. 4

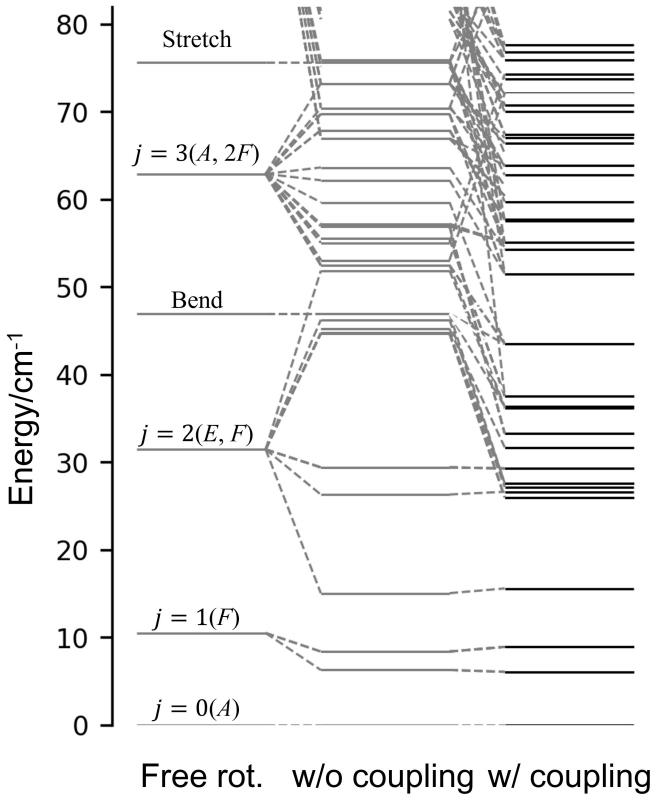

Fig. 7 Energy-level correlation diagram for the intermolecular vibration of Bz–methane. Left: the case for free internal rotation of methane with no mode coupling included. Middle: the case for hindered internal rotation for methane with no mode coupling included. Right: the case with all the potential terms included. Energies relative to the lowest level are represented. *A*, *E*, and *F* represent the symmetry due to methane internal rotation.

View Article Online
DOI: 10.1039/D5CP04295J

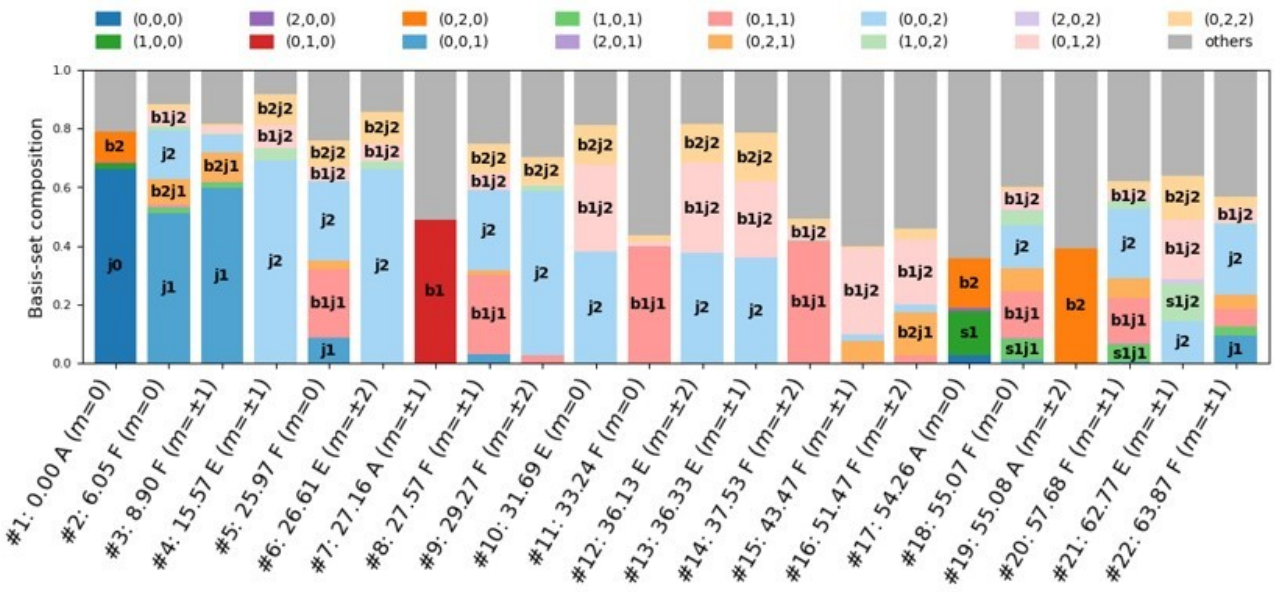

Fig. 8 Basis-function composition of each energy level with excitation energy up to 65 cm^{-1}. Basis functions are labeled as (n_0, v, j_X). In the graph, labeling as "s1" stands for $n_0 = 1$, "b1" for $v = 1$, "j1" for $j_X = 1$, and so on. Each state is labeled with ascending energy ordering, relative energy, symmetry, and m value.

sion. Then, molecules with different symmetry behave as if they are different molecular species (nuclear spin isomers).[44,48,49]

The diagonalization of the Hamiltonian matrices provided us the expansion coefficients for basis functions in each eigenstates obtained. Then, basis-set composition of each energy level is given as Fig. 8. As clearly seen in this figure, most of low-lying levels (with energy below 30 cm^{-1}) have their composition dominated (> 50%) by a single basis function. In particular, the levels of #1, #2, and #4 are the lowest in the A, E, and F manifolds, respectively, and they are well correlated to the hindered rotor states with $j_X = 0$, 1, and 2.

For levels lying higher in energy, we have to spend much care for state assignments, since they are mostly composed of several basis functions. Pure stretch or bend character is spread over among multiple levels. Let us consider levels assignable to the first excited states of the bend. In the A manifold, the #7 level is securely picked up as this kind of state, since it contains >50% character of the $v = 1$ state. For E and F, situation is not so straightforward. In the E manifold, states #10, #12, and #13 have larger $v = 1$ character but all of them contain a substantial pure internal-rotation component (with $j_X = 2$). This should be the results of the angular momentum coupling between bend and internal rotation. Four of F states (#5, #8, #11, and #14) have larger $v = 1$ character. The lower two also contain a substantial pure internal-rotation component (with $j_X = 2$), being another signature of angular momentum coupling. Since the states #5 and #11 belong to $m = 0$, it is practically impossible to make a unique assignment to the bend fundamental. Assignment of the first excited states of the stretch is also tedious. States #17 and #21 can be assignable to the stretch fundamental in the A and E manifolds, respectively, while states #18 and #20 to F, since the four states contain a perceivable contribution from the functions with $n_0 = 1$. However, the fractions of the stretch basis are far from dominant (< 20%), indicating the effects of substantial mode mixing.

By using the expansion coefficients for basis functions in each eigenstates obtained, we evaluated the averaged intermolecular distance $\langle R \rangle$, as well as the root-mean-square (RMS) amplitudes for the stretch, the bend, and the internal rotation: $\Delta R = \sqrt{\langle (R - R_e)^2 \rangle}$, $\Delta\rho = \sqrt{\langle \rho^2 \rangle}$, and $\Delta \cos\theta_X = \sqrt{\langle [\cos(\theta_X - \theta_{X,e}) - \langle \cos(\theta_X - \theta_{X,e}) \rangle]^2 \rangle}$, respectively. The results for each energy level below 65 cm^{-1} with $m \leq 2$ are listed in Table 6. From this list, the following notable points can be extracted.

For $\langle R \rangle$, the largest values of 3.68 Å, exhibited in the states with dominant internal-rotation characters (#1–4, #6, #9), are substantially shorter than that for the monodentate global minima (3.712 Å). This is an indication that the coupling between the stretch and the internal rotation (as shown in Fig. 6) is operative. The values for the states with some bend characters (#5, #7, #8, #10–16, #19) are further smaller (in the range of 3.62–3.65 Å). This may be rationalized by the stretch-bend-internal rotation coupling, where the methane becomes tilted as the bend coordinate becomes larger (as shown in Fig. 5), approaching to the bidentate conformation with preference of shorter R (3.634 Å). For the states with certain stretch characters (#17, #18, #20, #21), the distance is elongated to some extent (3.66–3.67 Å), definitely due to the anharmonicity of the stretch vibration.

The RMS amplitudes for the stretch, ΔR, are ~ 4% of the intermolecular distance R. The value of the states with dominant internal-rotation characters (#1–4, #6, #9) are 0.16 Å, and those for the states with some bend characters (#5, #7, #8, #10–16, #19) are slightly smaller (0.13–0.15 Å). The states with certain stretch characters (#17, #18, #20, #21) exhibit larger values of 0.17–0.18 Å), as expected.

The RMS amplitudes for the bend, $\Delta\rho$, fall within the range of 0.4–0.5 Å, which are 29–36% of the radius of the Bz ring (1.40 Å). In a classical point of view, the methane molecule is

View Article Online
DOI: 10.1039/D5CP04295J

Table 6 Intermolecular energy levels of Bz–methane up to 65 cm^{-1} with $|m| \leq 2$.

State No.	Symmetry	m	Energy/cm^{-1}	$\langle R \rangle$/Å	ΔR/Å	$\Delta\rho$/Å	$\Delta \cos\theta_X$
1	A	0	0.00	3.68	0.16	0.41	0.57
2	F	0	6.05	3.68	0.16	0.41	0.50
3	F	±1	8.90	3.68	0.16	0.41	0.57
4	E	±1	15.57	3.69	0.16	0.41	0.57
5	F	0	25.97	3.63	0.15	0.47	0.50
6	E	±2	26.61	3.68	0.16	0.41	0.57
7	A	±1	27.16	3.64	0.15	0.49	0.55
8	F	±1	27.57	3.64	0.15	0.47	0.52
9	F	±2	29.27	3.68	0.16	0.41	0.55
10	E	0	31.69	3.64	0.15	0.46	0.55
11	F	0	33.24	3.63	0.15	0.49	0.54
12	E	±2	36.13	3.64	0.15	0.47	0.56
13	E	±1	36.33	3.62	0.15	0.47	0.55
14	F	±2	37.53	3.65	0.15	0.49	0.54
15	F	±1	43.47	3.62	0.15	0.47	0.45
16	F	±2	51.47	3.62	0.14	0.47	0.52
17	A	0	54.26	3.67	0.18	0.39	0.51
18	F	0	55.07	3.67	0.18	0.42	0.45
19	A	±2	55.08	3.62	0.13	0.45	0.49
20	F	±1	57.68	3.67	0.17	0.42	0.50
21	E	±1	62.77	3.66	0.17	0.41	0.50
22	F	±1	63.87	3.67	0.16	0.40	0.52

sliding back and forth on the one-thirds of the Bz ring. The amplitudes of the states with bend characters (#5, #7, #8, #10–16, #19) are substantially larger (0.45–0.49 Å) that those for the states with internal-rotation characters (#1-4, #6, #9) (0.41 Å), as expected. The states with stretch characters (#17, #18, #20, #21) exhibit shorter values of 0.39–0.42 Å, similar to those with internal-rotation characters.

The limiting values of the RMS amplitudes for the internal rotation, $\Delta \cos\theta_X$, are zero in the rigid complex while $1/\sqrt{3} \sim 0.58$ in the case of free rotation. All the states listed in Table 6 exhibit slightly smaller values (ranging 0.45–0.57) than the free-rotation limit. In particular, the value (0.57) of several low-lying states (#1, #3, #4, #6) is very close to the free rotation limit. This is regarded reasonable since these states are dominated by a single internal-rotation basis function. The states #15 and #18 have the smallest value of 0.45. Such a reduction is an indication of partial localization of the internal-rotation wave functions.

5 Conclusions

In the present study, we have developed a new formalization, termed Coupled-Stretch-Bend-Internal-rotation (CSBI) model, to represent the IPS pertinent to vdW complexes, where a relatively small molecule X is attached on the surface of an aromatic molecule (e.g., Bz). The CSBI model takes the following three internal coordinates to describe the intermolecular vibration: the longitudinal displacement of X from the Bz plane (as vdW stretch), the 2D displacements of X parallel to the Bz ring (vdW bend), and the 3D internal rotation of X inside the complex. Then, the IPS is represented as a sum of symmetry-adapted terms, each of which is expressed as explicit functions of the coordinates. Even though the model is not suitable to describe complex configuration far off from the potential minima, it is capable to set out adequately any internal orientation of X. It also provides an appropriate description on the mode coupling among the three coordinates. In particular, angular momentum coupling between the 2D bend and the 3D internal rotation is formulated explicitly.

In the present report, we take Bz–methane as a suitable system to apply the CSBI approach because of its high symmetry and its significance as a prototypical model for the C–H/π interaction. Single-point energy calculation has been conducted at the CCSD(T)/aug-cc-pVTZ level of theory for 525 grids for various conformation of the complex, and the calculated results have been fit to determine potential parameters in the CSBI model. In The IPS thus constructed, the most stable geometry and the saddle points along the internal rotation have been allocated at the monodentate and bidentate conformations, respectively, between which the energy difference is moderately small (of 57 cm^{-1}). It has also been shown in the determined IPS that the internal rotation couples substantially with the bend and stretch modes, as clearly visualized in the 2D sections of the IPS shown in Figs. 3 and 4. Such an interlocking of the two modes is a dynamical outcome of the C–H/π interaction.

Based on the determined CSBI potential, eigenstates for the intermolecular motion of Bz–methane have been determined by diagonalizing the full Hamiltonian matrices, sorted with the A, E, and F symmetries and the coupled angular momentum component m for the bend and the internal rotation. The corresponding energy-level structure is highly congested, indicating the substantial effects of the mode coupling in the IPS. State characterization has been realized only after detailed examination of basis-function composition of each energy level. It has been shown characteristics of the levels are well correlated to the vibrationally averaged geometrical parameters, e.g., the intermolecular distance and the root-mean-square displacements for the internal coordinates. Such in-depth description of energy levels will be indispensable for comprehensive analysis of experimentally obtained data. We have already conducted frequency-

View Article Online
DOI: 10.1039/D5CP04295J

and time-domain spectroscopic investigation pertinent to the intermolecular vibration of Bz–methane. The analysis of the spectra is now underway and will be reported in a separate paper.

Author Contributions

Toru Sasaki: formal analysis, investigation, writing – original draft, and writing – review and editing. Masaaki Nakamura: investigation, validation, and writing – review and editing. Yasuhiro Ohshima: conceptualization, formal analysis, funding acquisition, investigation, validation, supervision, and writing – review and editing.

Conflicts of interest

There are no conflicts to declare.

Data availability

The data supporting this article have been included as part of Supplementary Information. See DOI: https://doi.org/10.1039/xxxxxxxxxx.

Acknowledgements

This work was supported by the JSPS KAKENHI Grants (JP15H03766, JP18H03897, JP20K21169, JP22H00312, JP22K18327, JP24KJ1071, and JP25K22240) and the JSPS Core-to-Core program (JPJSCCA20240002). The computation was performed using Research Center for Computational Science, Okazaki, Japan (Project: 22-IMS-C251).

References

1 O. Takahashi, Y. Kohno, S. Iwasaki, K. Saito, M. Iwaoka, S. Tomoda, Y. Umezawa, S. Tsuboyama and M. Nishio, *Bull. Chem. Soc. Jpn.*, 2001, **74**, 2421–2430.
2 E. A. Meyer, R. K. Castellano and F. Diederich, *Angew. Chem., Int. Ed.*, 2003, **42**, 1210–1250.
3 M. Nishio, *Phys. Chem. Chem. Phys.*, 2011, **13**, 13873–13900.
4 P. Hobza, H. L. Selzle and E. W. Schlag, *Chem. Rev.*, 1994, **94**, 1767–1785.
5 S. Sun and E. R. Bernstein, *J. Phys. Chem.*, 1996, **100**, 13348–13366.
6 B. Brutschy, *Chem. Rev.*, 2000, **100**, 3891–3920.
7 K. S. Kim, P. Tarakeshwar and J. L. Lee, *Chem. Rev.*, 2000, **100**, 4145–4185.
8 P. Hobza and K. Muller-Dethlefs, *Non-covalent Interactions: Theory and Experiment*, Royal Society of Chemistry, Cambridge, UK, 2009.
9 M. Schauer and E. Bernstein, *J. Chem. Phys.*, 1985, **82**, 726–735.
10 J. Menapace and E. Bernstein, *J. Phys. Chem.*, 1987, **91**, 2843–2848.
11 J. Menapace and E. Bernstein, *J. Phys. Chem.*, 1987, **91**, 2533–2544.
12 S.-i. Morita, A. Fujii, N. Mikami and S. Tsuzuki, *J. Phys. Chem. A*, 2006, **110**, 10583–10590.
13 K. Shibasaki, A. Fujii, N. Mikami and S. Tsuzuki, *J. Phys. Chem. A*, 2006, **110**, 4397–4404.
14 S. Sakaki, K. Kato, T. Miyazaki, Y. Musashi, K. Ohkubo, H. Ihara and C. Hirayama, *J. Chem. Soc., Faraday Trans.*, 1993, **89**, 659–664.
15 S. Tsuzuki, K. Honda, T. Uchimaru, M. Mikami and K. Tanabe, *J. Am. Chem. Soc.*, 2000, **122**, 3746–3753.
16 A. L. Ringer, M. S. Figgs, M. O. Sinnokrot and C. D. Sherrill, *J. Phys. Chem. A*, 2006, **110**, 10822–10828.
17 S. Tsuzuki and A. Fujii, *Phys. Chem. Chem. Phys.*, 2008, **10**, 2584–2594.
18 C. D. Sherrill, T. Takatani and E. G. Hohenstein, *J. Phys. Chem. A*, 2009, **113**, 10146–10159.
19 S. Tsuzuki, *Annu. Rep. Prog. Chem., Sect. C*, 2012, **108**, 69–95.
20 A. Stone, *The Theory of Intermolecular Forces*, Oxford University Press, Oxford, UK, 2nd edn., 2013.
21 W. Klopper, M. Quack and M. A. Suhm, *J. Chem. Phys.*, 1998, **108**, 10096–10115.
22 P. M. Felker and Z. Bačić, *J. Chem. Phys.*, 2019, **151**, 024305.
23 P. Jankowski, L. A. Surin, A. V. Potapov, S. Schlemmer, A. R. W. McKellar and K. Szalewicz, *J. Chem. Phys.*, 2013, **138**, 084307.
24 L. A. Surin, D. N. Fourzikov, T. F. Giesen, S. Schlemmer, G. Winnewisser, V. A. Panfilov, B. B. S. Dumesh, G. W. M. Vissers and A. van der Avoird, *J. Phys. Chem. A*, 2007, **111**, 12238–12247.
25 R. Dawes, X.-G. Wang and J. T. Carrington, *J. Phys. Chem. A*, 2013, **117**, 7612–7630.
26 C. Leforestier, K. Szalewicz and A. van der Avoird, *J. Chem. Phys.*, 2012, **137**, 014305.
27 J. Aling, K. Szalewicz and A. van der Avoird, *Nat. Comm.*, 2022, **13**, 1470.
28 O. Bludskỳ, V. Spirko, V. Hrouda and P. Hobza, *Chem. Phys. Lett.*, 1992, **196**, 410–416.
29 A. van der Avoird, *J. Chem. Phys.*, 1993, **98**, 5327–5336.
30 T. Brupbacher, J. Makarewicz and A. Bauder, *J. Chem. Phys.*, 1994, **101**, 9736–9746.
31 H. Koch, B. Fernández and J. Makarewicz, *J. Chem. Phys.*, 1999, **111**, 198–204.
32 S. B. Capelo, B. Fernandez, H. Koch and P. M. Felker, *J. Phys. Chem. A*, 2009, **113**, 5212–5216.
33 S. Lee, J. S. Chung, P. M. Felker, J. López Cacheiro, B. Fernández, T. Bondo Pedersen and H. Koch, *J. Chem. Phys.*, 2003, **119**, 12956–12964.
34 L. Shirkov and J. Makarewicz, *J. Chem. Phys.*, 2015, **142**, 204107.
35 L. Shirkov, *J. Phys. Chem. A*, 2024, **128**, 6132–6139.
36 P. M. Felker, *J. Chem. Phys.*, 2001, **114**, 7901–7910.
37 S. Lee, J. Romascan, P. M. Felker, T. B. Pedersen, B. Fernández and H. Koch, *J. Chem. Phys.*, 2003, **118**, 1230–1241.

View Article Online
DOI: 10.1039/D5CP04295J

38 W. Kim, D. Neuhauser, M. R. Wall and P. M. Felker, *J. Chem. Phys.*, 1999, **110**, 8461–8475.

39 P. M. Felker and Z. Bačić, *J. Chem. Phys.*, 2020, **152**, 124103.

40 A. van der Avoird, P. E. Wormer and R. Moszynski, *Chem. Rev.*, 1994, **94**, 1931–1974.

41 P. R. Bunker and P. Jensen, *Molecular Symmetry and Spectroscopy*, NRC Research Press, Ottawa, Canada, 2nd edn., 1998.

42 P. M. Felker, D. Neuhauser and W. Kim, *J. Chem. Phys.*, 2001, **114**, 1233–1241.

43 R. N. Zare, *Angular Momentum: Understanding Spatial Aspects in Chemistry and Physics*, Wiley Interscience, 1988.

44 T. G. Heil and D. Secrest, *J. Chem. Phys.*, 1978, **69**, 219–230.

45 L. N. Smith, D. J. Malik and D. Secrest, *J. Chem. Phys.*, 1979, **71**, 4502–4514.

46 L. N. Smith and D. Secrest, *J. Chem. Phys.*, 1981, **74**, 3882–3897.

47 Y. Ohshima and Y. Endo, *J. Chem. Phys.*, 1990, **93**, 6256–6265.

48 R. W. Randall, J. B. Ibbotson and B. J. Howard, *J. Chem. Phys.*, 1994, **100**, 7042–7050.

49 T. G. Heijmen, P. E. Wormer, A. van der Avoird, R. E. Miller and R. Moszynski, *J. Chem. Phys.*, 1999, **110**, 5639–5650.

50 M. J. Frisch, G. W. Trucks, H. B. Schlegel, G. E. Scuseria, M. A. Robb, J. R. Cheeseman, G. Scalmani, V. Barone, G. A. Petersson, H. Nakatsuji, X. Li, M. Caricato, A. V. Marenich, J. Bloino, B. G. Janesko, R. Gomperts, B. Mennucci, H. P. Hratchian, J. V. Ortiz, A. F. Izmaylov, J. L. Sonnenberg, D. Williams-Young, F. Ding, F. Lipparini, F. Egidi, J. Goings, B. Peng, A. Petrone, T. Henderson, D. Ranasinghe, V. G. Zakrzewski, J. Gao, N. Rega, G. Zheng, W. Liang, M. Hada, M. Ehara, K. Toyota, R. Fukuda, J. Hasegawa, M. Ishida, T. Nakajima, Y. Honda, O. Kitao, H. Nakai, T. Vreven, K. Throssell, J. J. A. Montgomery, J. E. Peralta, F. Ogliaro, M. J. Bearpark, J. J. Heyd, E. N. Brothers, K. N. Kudin, V. N. Staroverov, T. A. Keith, R. Kobayashi, J. Normand, K. Raghavachari, A. P. Rendell, J. C. Burant, S. S. Iyengar, J. Tomasi, M. Cossi, J. M. Millam, M. Klene, C. Adamo, R. Cammi, J. W. Ochterski, R. L. Martin, K. Morokuma, O. Farkas, J. B. Foresman and D. J. Fox, *Gaussian 16, Revision C.01*, Gaussian, Inc., Wallingford, CT, 2016.

51 G. D. Purvis and R. J. Bartlett, *J. Chem. Phys.*, 1982, **76**, 1910–1918.

52 K. Raghavachari, G. W. Trucks, J. A. Pople and M. Head-Gordon, *Chem. Phys. Lett.*, 1989, **157**, 479–483.

53 T. H. Dunning, Jr., *J. Chem. Phys.*, 1989, **90**, 1007–1023.

54 R. A. Kendall, T. H. Dunning, Jr. and R. J. Harrison, *J. Chem. Phys.*, 1992, **96**, 6796–6806.

55 D. G. Smith and K. Patkowski, 2013, **9**, 370–389.

56 M. B. Oviedo, N. V. Ilawe and B. M. Wong, 2016, **12**, 3593–3602.

57 J. J. Sakurai and J. Napolitano, *Modern Quantum Mechanics*, Cambridge University Press, Cambridge, 2nd edn., 2017.

58 A. Messiah, in *Quantum Mechanics*, Dover Publications, Mineola, NY, Unabridged republication; two volumes bound as one edn., 2014, ch. 12.

59 P. M. Maxton, M. W. Schaeffer, S. M. Ohline, W. Kim, V. A. Venturo and P. M. Felker, *J. Chem. Phys.*, 1994, **101**, 8391–8408.

60 G. Tarrago, M. Dang-Nhu, G. Poussigue, G. Guelachvili and C. Amiot, *J. Mol. Spectrosc.*, 1975, **57**, 246–263.

61 A. Doi, M. Baba, S. Kasahara and H. Katô, *J. Mol. Spectrosc.*, 2004, **227**, 180–186.

62 E. Anderson, Z. Bai, C. H. Bischof, S. Blackford, J. Demmel, J. Dongarra, J. Du Croz, A. Greenbaum, S. Hammarling, A. McKenney and D. Sorensen, *LAPACK Users' Guide*, Society for Industrial and Applied Mathematics, Philadelphia, PA, 3rd edn., 1999.

View Article Online
DOI: 10.1039/D5CP04295J

The data supporting this article have been included as part of Supplementary Information.